Using Photometrically Derived Properties of Young Stars to Refine TESS's Transiting Young Planet Survey Completeness

Rachel B. Fernandes[1,2,3,4,15] , Kevin K. Hardegree-Ullman[4,5] , Ilaria Pascucci[3,4] , Galen J. Bergsten[3,4] ,
Gijs D. Mulders[4,6,7] , Katia Cunha[8,9,10] , Eric E. Mamajek[11,12] , Kyle A. Pearson[11] , Gregory A. Feiden[13] , and
Jason L. Curtis[14]

[1] Department of Astronomy & Astrophysics, Center for Exoplanets and Habitable Worlds, The Pennsylvania State University, University Park, PA 16802,
USA; rachelfernandes@arizona.edu
[2] Center for Exoplanets and Habitable Worlds, 525 Davey Laboratory, The Pennsylvania State University, University Park, PA 16802, USA
[3] Lunar and Planetary Laboratory, The University of Arizona, Tucson, AZ 85721, USA
[4] Alien Earths Team, NASA Nexus for Exoplanet System Science, USA
[5] Steward Observatory, The University of Arizona, Tucson, AZ 85721, USA
[6] Facultad de Ingeniería y Ciencias, Universidad Adolfo Ibáñez, Av. Diagonal las Torres 2640, Peñalolén, Santiago, Chile
[7] Millennium Institute for Astrophysics, Chile
[8] Observatório Nacional/MCTIC, R. Gen. José Cristino, 77, 20921-400, Rio de Janeiro, Brazil
[9] Steward Observatory, University of Arizona, 933 North Cherry Avenue, Tucson, AZ 85721-0065, USA
[10] Institut dAstrophysique de Paris, UMR7095 CNRS, Sorbonne Université, 98bis Bd. Arago, F-75014 Paris, France
[11] Jet Propulsion Laboratory, California Institute of Technology, 4800 Oak Grove Drive, Pasadena, CA 91109, USA
[12] Department of Physics and Astronomy, University of Rochester, Rochester, NY 14627-0171, USA
[13] Department of Physics and Astronomy, University of North Georgia, Dahlonega, GA 30597 USA
[14] Department of Astronomy, Columbia University, 550 West 120th Street, New York, NY 10027, USA

Abstract

The demographics of young exoplanets can shed light on their formation and evolution processes. Exoplanet properties are derived from the properties of their host stars. As such, it is important to accurately characterize the host stars since any systematic biases in their derivation can negatively impact the derivation of planetary properties. Here we present a uniform catalog of photometrically derived stellar effective temperatures, luminosities, radii, and masses for 4865 young (<1 Gyr) stars in 31 nearby clusters and moving groups within 200 pc. We compared our photometrically derived properties to a subset of those derived from spectra and found them to be in good agreement. We also investigated the effect of stellar properties on the detection efficiency of transiting short-period young planets with TESS as calculated in Fernandes et al. (2022) and found an overall increase in the detection efficiency when the new photometrically derived properties were taken into account. Most notably, there is a $1.5 \times$ increase in the detection efficiencies for sub-Neptunes/Neptunes ($1.8–6\,R_\oplus$) implying that, for our sample of young stars, better characterization of host star properties can lead to the recovery of more small transiting planets. Our homogeneously derived catalog of updated stellar properties, along with a larger unbiased stellar sample and more detections of young planets, will be a crucial input to the accurate estimation of the occurrence rates of young short-period planets.

1. Introduction

The discovery of thousands of transiting exoplanets via large-scale surveys such as Kepler (Borucki et al. 2010), K2 (Howell et al. 2014), and TESS (Ricker et al. 2014) has enabled us to explore not only individual planets and systems but also planet populations. However, the determination of exoplanet properties is dependent on robust knowledge of their host stars, most notably stellar radii, masses, and effective temperatures, which can be used to derive planet radii, masses, and equilibrium temperatures. In order to facilitate target selection, catalogs providing basic stellar properties were developed for

Kepler, K2, and TESS, such as the Kepler Input Catalog (KIC; Brown et al. 2011), the Ecliptic Plane Input Catalog (EPIC; Huber et al. 2016), and the TESS Input Catalog (TIC; Stassun et al. 2018), respectively. These input catalogs were derived by combining data from heterogeneous sources and hence cannot be used as a precise reference for stellar properties and exoplanet demographics.

For studies of exoplanet populations, it is especially crucial to have a homogeneously derived stellar catalog, as any systematic biases in the derivation of the stellar properties can negatively impact the derivation of planetary properties and therefore lead to the incorrect characterization of the planet populations. One prominent example is the discovery of the radius valley in Kepler's short-period small-planet population, which was enabled by uniform spectroscopic (Fulton et al. 2017) and astroseismic (Van Eylen et al. 2018) stellar classification. The Gaia mission (Gaia Collaboration et al. 2016) has transformed the field of stellar classification,

---

[15] President's Postdoctoral Fellow.

providing photometry and distances to over a billion stars (Gaia Collaboration et al. 2018, 2021). With Gaia DR2 data, Berger et al. (2020) and Hardegree-Ullman et al. (2020) were able to update the Kepler and K2 stellar catalogs, respectively, in a homogeneous manner, with the latter enabling the confirmation of the planet radius valley beyond the Kepler field. Stassun et al. (2019) also incorporated Gaia DR2 data into the TIC. However, there are still many inhomogeneities in the derivation of TIC stellar properties, so it should not be used for large-scale exoplanet demographic studies. A fully uniform catalog of TESS stellar properties for nearly two billion stars is a difficult task, but uniform catalogs of subsets of TESS targets are a much more tractable goal.

While most known short-period transiting exoplanets have been found orbiting Gyr-old stars, over the past decade K2 and TESS have facilitated the discovery of >30 young (<1 Gyr) exoplanets (A. Vanderburg 2023, private communication; e.g., Newton et al. 2019; Bouma et al. 2020; Mann et al. 2020; Nardiello et al. 2020; Rizzuto et al. 2020; Newton et al. 2021). The discovery and characterization of young short-period exoplanets is crucial to our understanding of planet formation and evolution processes such as photoevaporation (e.g., Owen & Wu 2013, 2017) and core-powered mass loss (e.g., Ginzburg et al. 2016, 2018; Gupta & Schlichting 2019, 2020, 2020). Young stellar clusters and moving groups are promising targets to search for such planets. TESS enables this search by providing light curves spanning nearly the entire sky. However, if we hope to learn about the demographics of young planets, we still need a uniform catalog of stellar properties. Young stars are typically still evolving onto the main sequence, so their properties cannot necessarily be derived using the same assumptions, inputs, or relationships as their main-sequence counterparts. While past studies of individual young clusters and associations have yielded stellar properties for those clusters (e.g., Fang et al. 2023), we aim to study planets in all known nearby young clusters and associations (within 200 pc), and this necessitates a larger homogeneous catalog.

Ideally, we would have a spectrum for each star to yield precise spectral type, effective temperature, surface gravity, and metallicity information. However, less than 10% of our sample of young stars have spectra, and so we must depend on available photometry to characterize these stars. Here we present a uniformly derived catalog of photometrically derived stellar properties for 4865 stars in nearby (within 200 pc) young clusters and moving groups. In Section 2, we use data from Gaia DR3 to derive stellar effective temperatures, luminosities, radii, and masses. We test our derived stellar properties by comparing them to properties measured from spectra for a subset of our sample in Section 3. Next, we use our stellar catalog to update the detection efficiency analysis and planet occurrence rate calculations for young stars from Fernandes et al. (2022) in Section 4. Finally, we summarize our results and discuss the next steps needed to further improve our stellar catalog and planet occurrence rates for young stars in Section 5.

2. Stellar Classification

The focus of this work is to compute a homogeneous catalog of stellar T_{eff}, radii, and masses to aid in the accurate estimation of young transiting exoplanet radii, as well as to place constraints on their demographics. Given that TESS decreases in sensitivity to transiting planets orbiting fainter low-mass stars (e.g., Dietrich et al. 2023), we only classified stars of F, G, K, and early M

spectral types (down to M3.5 V), as they are typically bright enough and have a higher chance of hosting a detectable planet with TESS.

Our sample of nearby moving groups and young clusters was compiled using the BANYAN Σ (Gagné et al. 2018) and the Gaia DR2 open cluster member lists (Gaia Collaboration, Babusiaux et al. 2018). We also added the more recently discovered Argus (Zuckerman 2019), MUTA (Gagné et al. 2020), and Pisces-Eridanus (Curtis et al. 2019) groups. We restricted the median moving group or young cluster distance to ~200 pc to ensure that we can detect planets around later K- and early M-type stars with TESS. We excluded clusters younger than 10 Myr since their stars could still retain a disk (e.g., Ercolano & Pascucci 2017) and their light curves are highly complex and variable (e.g., Cody et al. 2014). We included clusters up to 1 Gyr to cover ages over which the short-period planet population is expected to evolve (e.g., Rogers et al. 2021). With these distance and age cuts, we obtained a starting sample of 10,585 young stars from 31 young clusters and moving groups (see Table 3 in the Appendix).

2.1. Main-sequence versus Pre-main-sequence Sample

The age at which any given star reaches the main sequence depends on its stellar mass: a 1.6 $M_\odot$ F-type star takes ~20 Myr to reach the main sequence, whereas a 0.1 $M_\odot$ M dwarf (like TRAPPIST-1) can take up to a billion years. However, the majority of our sample of young stars do not have measured masses, which makes it challenging to determine which stars in a given cluster are pre-main-sequence and which stars have already reached the main sequence. To combat this, we relied on G-, G_{BP}-, and G_{RP}-band magnitudes for our targets from Gaia DR3 (Gaia Collaboration et al. 2023b), along with distances from Bailer-Jones et al. (2021) and Two Micron All Sky Survey (2MASS) IDs and photometry (Skrutskie et al. 2006) from Gaia's best neighbor cross-match (see Table 3 in the Appendix). At this stage, we removed all targets with nonfinite magnitudes, parallaxes, and associated errors since we could not compute stellar properties for them, leaving us with 10,238 targets.

In crowded fields (typical in young cluster environments), it is highly probable that a given exoplanet transit is diluted owing to the light from a bound companion star, which can lead to an underestimated planet radius measurement. To this effect, we identified and removed any known binaries and nonsingle sources in our sample using the Gaia EDR3 binary catalog (El-Badry et al. 2021), the Robo-AO census of companions within 25 pc (Salama et al. 2022), and the Gaia DR3 non-single-star catalog (Gaia Collaboration et al. 2023a), leaving us with 9462 targets. Gaia also provides a Renorma-lised Unit Weight Error (RUWE) score for each source. For sources where the astrometric observations fit well with the single-star model, the expected RUWE value is around 1.0. However, a value greater than 1.0 suggests that the source either could be nonsingle or has other issues that may affect the accuracy of the astrometric solution. Targets with an RUWE score >1.4 have been found to be indicative of a nonsingle source (Ziegler et al. 2020). As such, we also removed any stars with a Gaia DR3 RUWE score >1.4, which left us with 8239 stars for which stellar properties could be computed.

Here, it is important to note that although we removed all known binaries and sources with high RUWE scores from our sample, there is still a possibility of unresolved binaries leading

to improper star classification. For instance, if a G-type main-sequence star has an unresolved equal-mass binary, the photometric colors would not be affected, but the combined flux from both stars would lead to an overestimation of the system's luminosity. This overestimation of the luminosity would propagate into the mass and radius estimates derived from the luminosity, leading to an overestimation of both quantities. Since pre-main-sequence stars are more luminous and have larger radii, the mischaracterization of a main-sequence star as pre-main-sequence could occur if there is an unresolved binary. This mischaraterization would further propagate into the derivation of the planet radii. More specifically, an equal-mass binary would cause the luminosity to be overestimated by $2\times$. This means that the radius of the star as derived from the flux would be $\sqrt{2}\times$ larger than the true radius. This would cause the transit depth of the planet to be diluted by $0.5\times$ and the radius of the planet to be under-estimated by $\sqrt{2}\times$ or approximately 41.42%. Assuming a stellar multiplicity rate of 44% and 26% for FGK and M stars, respectively (Duchêne & Kraus 2013), and given that our previous known binary and high RUWE score cuts removed ~20% of the sample, we are left with a possible $\sim292-1168$ unresolved binaries in our sample that are likely mischaracterized. Dilution resulting from unresolved binaries is also expected to hinder our ability to detect the transit signals of smaller planets, ultimately reducing our detection efficiency within those particular bins. To address this issue, performing a thorough assessment of the multiplicity of each star in our sample would be ideal. However, it would necessitate extensive ground-based follow-up using high-resolution imaging, which is beyond the scope of this paper.

Using the intrinsic color of a star, i.e., the difference in magnitude calculated using two different color filters, along with the absolute magnitude, we created a Hertzsprung–Russell diagram (Hertzsprung 1911; Russell 1914) to differentiate between the pre-main-sequence and main-sequence stars (see Figure 1).

Here we used Gaia DR3 and 2MASS photometry of the standard main-sequence stars that were used to create Table 5[16] in Pecaut & Mamajek (2013, hereafter PM13) in order to establish M_{K_S} versus $G_{BP} - G_{RP}$ or $G - G_{RP}$ relationships. We determined the main-sequence by fitting a fifth-order polynomial to M_{K_S} and $G_{BP} - G_{RP}$. The polynomial order for each of the fits in this paper was the lowest order needed to fit large-scale structure while higher orders did not significantly improve the rms residual scatter. Since G_{BP} is not well constrained for intrinsically redder stars, we instead fit M_{K_S} and $G - G_{RP}$ with a fifth-order polynomial for targets with $4.5 < M_{K_S} < 10$. All stars within 10% of both these fits are analyzed as main-sequence stars in this work, while the rest were analyzed as pre-main-sequence, i.e., stars of a given color are labeled as main-sequence if their magnitude is within 10% of that found by evaluating the main-sequence best-fit polynomial at that color. At this point, we also removed stellar populations that we could not accurately classify for both main-sequence and pre-main-sequence populations:[17] white dwarfs and OBA stars ($0.5 < G_{BP} - G_{RP} < 3.5$), and late M stars ($M_{K_S} > 7.1$). These cuts gave us a total population of 4865
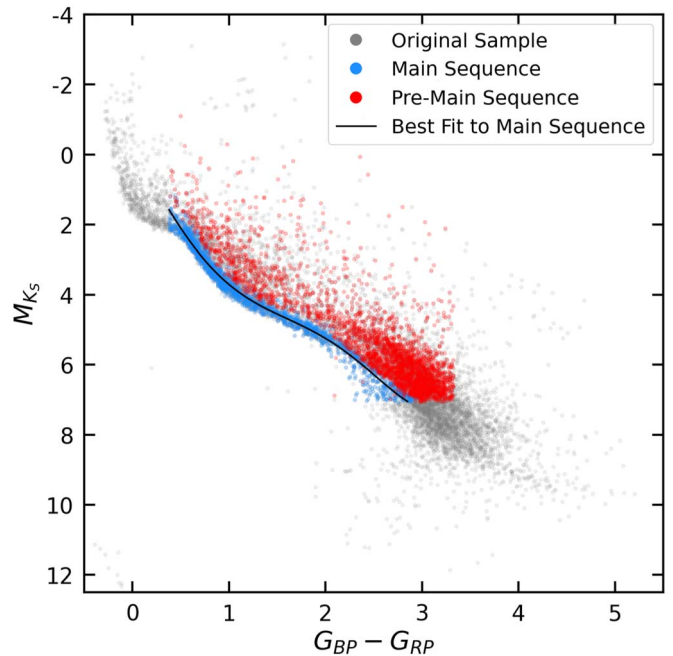

Figure 1. Hertzsprung–Russell diagram of our starting sample of stars from 31 young clusters and moving groups (gray). Stars classified in this work as pre-main-sequence and main-sequence stars are also shown in red and blue, respectively. Around $M_{K_S} = 2$ mag there is an apparent bifurcation in the main-sequence stars. The sparsity of data points in that region for which to fit our color–magnitude polynomial could lead to some misclassification of pre-main-sequence stars as main-sequence stars, which we think is happening here.

stars (1824 main-sequence, and 3041 pre-main-sequence) for which we derived stellar properties (see Figure 1).

2.2. Stellar Effective Temperatures and Radii

Using intrinsic colors, we can derive stellar effective temperature (hereafter T_{eff}). The T_{eff} for pre-main-sequence stars was computed by fitting a seventh-degree polynomial to the derived $G_{BP} - G_{RP}$ colors and T_{eff} for pre-main-sequence stars from Table 6 in PM13. We note that the PM13 pre-main-sequence table does not have Gaia color information, but it has $V - I_c$ colors, which we converted to $G_{BP} - G_{RP}$ using Gaia photometric relations with other photometric catalogs (Busso et al. 2021). For main-sequence stars, we fit a fourth-order polynomial to $G_{BP} - G_{RP}$ versus T_{eff} from the set of individual measurements from standard stars used to create the most recent version of Table 5 in PM13.

All uncertainties herein were calculated using a Monte Carlo method. For T_{eff}, we started with each G_{BP} and G_{RP} magnitude and associated error, drew a normal distribution of 1000 points, computed $G_{BP} - G_{RP}$ from those posteriors, ran the $G_{BP} - G_{RP}$ posterior through the polynomial fit, and took the median value of the resultant distribution as our T_{eff}. We added the standard deviation of the T_{eff} distribution in quadrature to the ~1% and ~1.66% rms deviation from the polynomial fits for pre-main-sequence and main-sequence stars, respectively. The median uncertainties on T_{eff} are 1.34% and 2.67% for pre-main-sequence and main-sequence stars, respectively. The main-sequence T_{eff} uncertainties are larger because there were significantly more data points used for that polynomial fit, resulting in a larger rms scatter. Our T_{eff} uncertainties are likely underestimated, but they are the best we can do given the data

---

[16] An updated version is maintained at https://www.pas.rochester.edu/ẽmamajek/EEM_dwarf_UBVIJHK_colors_Teff.txt.

[17] Table 6 of PM13 is only complete to M5 pre-main-sequence stars, which we used as a guide for our color and magnitude limits.

we have for our polynomial fits. We urge caution using these T_{eff} uncertainties for individual targets.

In Section 2.1, we used M_{K_S} magnitudes to define our sample of main and pre-main-sequence stars, particularly to help establish cutoffs for late M dwarfs. Since we are classifying stars from F to early M, we chose to apply bolometric corrections in the optical G band to minimize these corrections across different spectral types. We calculated the bolometric magnitude using the absolute G magnitude (M_G), the bolometric correction in G band (BC_G), and the total extinction in G band (A_G) as in the equation below:

$$M_{\text{bol}} = M_G + \text{BC}_G - A_G. \tag{1}$$

Since we did not immediately have a value for BC_G, we converted PM13's BC_J to BC_G. We first fit a 7th degree polynomial to the $G_{\text{BP}} - G_{\text{RP}}$ colors we computed earlier and BC_J from Table 6 in PM13 and used that relation to compute BC_J for our targets. Then we converted BC_J to BC_G with $\text{BC}_G = \text{BC}_J - (m_G - m_J)$, where m_G and m_J are the apparent magnitudes in Gaia G and 2MASS J bands, respectively. We then computed the bolometric luminosity as follows:

$$L_{\text{bol}} = L_0 \times 10^{-0.4 \times M_{\text{bol}}}, \tag{2}$$

where $L_0 = 3.0128 \times 10^{28}$ W is an IAU value also used in Mamajek et al. (2015). We accounted for extinction in each band by computing reddening using the `dustmaps` code (Green 2018). For targets north of $-30°$ in decl., we used the most recent Bayestar map (Green et al. 2019) to compute reddening in J band and converted it to extinction by multiplying the value by 0.7927 from Table 1 of Green et al. (2019). For targets south of $-30°$ in decl., which the Bayestar map does not cover since it was calibrated using data from the northern hemisphere Pan-STARRS survey, we used the recalibrated Schlegel et al. (1998) dust map from Schlafly & Finkbeiner (2011). For these targets we computed $E(B - V)$ using `dustmaps` and converted it to A_V extinction by multiplying the value by 2.742 (assuming $R_V = 3.1$) from Table 6 of Schlafly & Finkbeiner (2011). We then converted A_J and A_V to extinction in other bands by multiplying our values by those listed in Table 3 of Wang & Chen (2019), again assuming $R_V = 3.1$. Since our targets are typically within 200 pc, the effect of extinction is minimal (median $A_V = 0.03$ mag, $A_J = 0.007$ mag), so we are not concerned about using two different dust maps for northern and southern targets, or converting extinctions to different bands.

Using our T_{eff} and luminosity values, we then computed stellar radius using the Stefan–Boltzmann law:

$$R_\star = \sqrt{\frac{L_{\text{bol}}}{4\pi\sigma_{\text{SB}}T_{\text{eff}}^4}}, \tag{3}$$

where σ_{SB} is the Stefan–Boltzmann constant. However, for lower-mass or "redder" targets in the range $4.5 < M_{K_S} < 7.1$, the stellar radii were computed using the magnitude–radius relationship from Mann et al. (2015). This magnitude–radius relationship was calibrated using 183 well-characterized nearby K7–M7 single stars and yields radius uncertainties of $\sim 3\%$ for the above M_{K_S} magnitude range. FGK stars have higher median radius uncertainties of 3.7% and 5.7% for pre-main-sequence and main-sequence stars, respectively, but we again urge

caution with these uncertainties since they depend partially on our low T_{eff} uncertainties.

2.3. Stellar Masses

In order to derive stellar masses for the main-sequence stars in our sample, we used the mass–luminosity relation from Torres et al. (2010) for stars with $\log(L_\star/L_\odot) > -1$, which corresponds to a mass $M_\star \gtrsim 0.7\,M_\odot$. For targets with $\log(L_\star/L_\odot) < -1$ and in the range $4.5 < M_{K_S} < 7.1$, we computed masses from the empirical magnitude–mass relationship from Mann et al. (2019).

The masses of pre-main-sequence stars were derived using stellar evolutionary tracks (e.g., Fang et al. 2021). For this work, we converted the IDL code developed by Pascucci et al. (2016) into Python. This code uses a Bayesian inference approach to estimate stellar mass, age, and associated uncertainties from the stellar T_{eff}, L_{bol}, and a set of isochrones. The conditional likelihood function assumes uniform priors on the model properties, and we propagated uncertainties on T_{eff} and L_{bol} from our photometric derivations. We used the nonmagnetic Feiden (2016) tracks to ages as old as 500 Myr and included new tracks for magnetically active stars. These new tracks are more appropriate for young M dwarfs ($M_\star \lesssim 0.5\,M_\odot$) as shown, for example, by Simon et al. (2019), who compared masses from evolutionary tracks to dynamical masses and found that nonmagnetic tracks systematically underestimate the pre-main-sequence M dwarf masses by $\sim 50\%$.

3. Stellar Catalog Validation

Our homogeneous catalog of photometrically derived T_{eff}, $L_\star$, $R_\star$, and $M_\star$ for pre-main-sequence and main-sequence stars can be found in Tables 1 and 2. In the following sections, we performed a few validation checks of our derived stellar properties against those derived by other methods.

3.1. Comparison between Photometric and Spectroscopic Stellar Properties

To test the reliability of our photometrically derived properties, we compared them to values from the GALAH DR3 (Buder et al. 2021), APOGEE DR17 (Abdurrouf & Aerts 2022), and LAMOST DR8[18] (Cui et al. 2012) survey catalogs. For each survey, we imposed some simple quality cuts. For GALAH, we used the recommended quality cuts[19] of signal-to-noise ratio (S/N) > 30 in channel 3 and stellar parameter and iron abundance flags equal to zero, indicating no known problems with derived stellar properties. For APOGEE, we imposed a cut requiring no flags on stellar parameters (`STARFLAG=0`). For LAMOST, we imposed an S/N cut in g band for AFGK stars and in i band for M stars between 20 and 999 and made sure that errors for T_{eff}, $\log g$, and [Fe/H] or [M/H] were not –9999, the default value for poor-quality measurements.

Each spectroscopic catalog contains Gaia DR3 IDs, so we cross-matched our TESS targets to each catalog based on this ID. For our main-sequence sample, this yielded an overlap of 172 GALAH targets, 163 APOGEE targets, 356 LAMOST AFGK targets, and 178 LAMOST M targets. For our pre-main-

---

Table 1
Pre-main-sequence Stellar Properties

TIC	Cluster	Distance (pc)	T_{eff} (K)	$\log L_\star$ ($L_\odot$)	$R_\star$ ($R_\odot$)	$M_\star$ (Nonmag) ($M_\odot$)	$M_\star$ (Mag) ($M_\odot$)
138901588	32Ori	$100.097^{+0.210}_{-0.244}$	3209 ± 42	-1.414 ± 0.020	0.521 ± 0.018	$0.174^{+0.280}_{-0.174}$	$0.302^{+0.320}_{-0.302}$
302417238	32Ori	$91.507^{+0.271}_{-0.229}$	3277 ± 44	-1.673 ± 0.018	0.422 ± 0.014	$0.204^{+0.296}_{-0.204}$	$0.372^{+0.325}_{-0.372}$
365747593	32Ori	$98.177^{+0.153}_{-0.126}$	5743 ± 79	0.227 ± 0.018	1.311 ± 0.044	$1.202^{+0.277}_{-0.194}$	$1.122^{+0.181}_{-0.026}$
449260853	32Ori	$91.516^{+0.155}_{-0.154}$	3183 ± 42	-1.298 ± 0.019	0.578 ± 0.019	$0.162^{+0.276}_{-0.162}$	$0.275^{+0.317}_{-0.275}$
455029978	32Ori	$27.625^{+0.018}_{-0.019}$	3221 ± 43	-1.541 ± 0.019	0.465 ± 0.015	$0.174^{+0.284}_{-0.174}$	$0.309^{+0.327}_{-0.309}$
19699155	118Tau	$108.085^{+0.226}_{-0.207}$	5379 ± 74	0.559 ± 0.019	2.192 ± 0.077	$1.862^{+1.201}_{-1.115}$	$1.549^{+0.713}_{-0.606}$
54006139	118Tau	$87.904^{+0.139}_{-0.131}$	4594 ± 62	-0.277 ± 0.018	1.149 ± 0.040	$1.047^{+0.072}_{-0.024}$	$0.955^{+0.022}_{-0.066}$
54185108	118Tau	$106.563^{+0.201}_{-0.189}$	3216 ± 43	-0.875 ± 0.812	0.620 ± 0.020	$0.195^{+0.292}_{-0.195}$	$0.302^{+0.313}_{-0.302}$
62632828	118Tau	$95.540^{+0.289}_{-0.357}$	3063 ± 52	-1.727 ± 0.020	0.410 ± 0.014	$0.105^{+0.227}_{-0.105}$	$0.191^{+0.285}_{-0.191}$
1364042	ABDMG	$44.350^{+0.029}_{-0.033}$	3273 ± 44	-1.632 ± 0.019	0.434 ± 0.014	$0.204^{+0.296}_{-0.204}$	$0.372^{+0.317}_{-0.372}$

(This table is available in its entirety in machine-readable form.)

Table 2
Main-sequence Stellar Properties

TIC	Cluster	Distance (pc)	T_{eff} (K)	$\log L_\star$ ($L_\odot$)	$R_\star$ ($R_\odot$)	$M_\star$ ($M_\odot$)
4069456	32Ori	$41.708^{+0.026}_{-0.024}$	5290 ± 141	-0.317 ± 0.013	0.824 ± 0.047	0.823 ± 0.065
11085881	32Ori	$172.279^{+1.746}_{-1.616}$	3454 ± 92	-1.796 ± 0.017	0.363 ± 0.013	0.352 ± 0.012
147799311	32Ori	$111.591^{+0.134}_{-0.134}$	5932 ± 158	0.239 ± 0.015	1.248 ± 0.067	1.119 ± 0.088
284864375	32Ori	$58.250^{+0.055}_{-0.051}$	3836 ± 102	-1.117 ± 0.016	0.607 ± 0.020	0.598 ± 0.019
371691843	32Ori	$36.780^{+0.022}_{-0.017}$	3411 ± 91	-1.888 ± 0.015	0.334 ± 0.011	0.314 ± 0.010
408042385	32Ori	$44.120^{+0.046}_{-0.047}$	6273 ± 168	0.234 ± 0.015	1.109 ± 0.062	1.118 ± 0.088
433143783	32Ori	$49.707^{+0.060}_{-0.058}$	4809 ± 129	-0.655 ± 0.015	0.680 ± 0.038	0.683 ± 0.054
443750439	32Ori	$55.825^{+0.078}_{-0.075}$	3253 ± 87	-2.012 ± 0.014	0.308 ± 0.010	0.286 ± 0.009
6749695	118Tau	$54.639^{+0.057}_{-0.044}$	3686 ± 98	-1.228 ± 0.015	0.572 ± 0.018	0.568 ± 0.018
60511067	118Tau	$51.610^{+0.042}_{-0.047}$	3312 ± 88	-1.791 ± 0.016	0.370 ± 0.013	0.358 ± 0.011

(This table is available in its entirety in machine-readable form.)

sequence sample, this yielded an overlap of 21 GALAH targets, 71 APOGEE targets, 97 LAMOST AFGK targets, and 589 LAMOST M targets. As can be seen in Figure 2, there is agreement between spectroscopically and photometrically derived temperatures for main-sequence stars above ∼4000 K, where the standard deviation of the difference in T_{eff} is 138 K, about the same as our 149 K median T_{eff} uncertainty for these stars. Photometric T_{eff} values for main-sequence stars below ∼4000 K are on average 118 K lower than the spectroscopic measurements, which is slightly higher than our median T_{eff} uncertainty of 93 K for these cool stars. Andrae et al. (2018) and Dressing et al. (2019) identified a similar trend and suggested either extinction or strong molecular features in M dwarfs causing the discrepancy. Since we do not see a similar T_{eff} offset for warmer stars, we assume that the most likely cause is due to the strong molecular features in M dwarfs, which can make it difficult to fit precise stellar parameters, rather than extinction. Pre-main-sequence stars typically have higher spectroscopic T_{eff} values than photometric values. The likely cause of this discrepancy is the use of main-sequence stellar models in the spectroscopic parameter fitting, which are not necessarily appropriate for most young stars.

We also compared our stellar properties with those derived by Román-Zúñiga et al. (2023) using spectra from APOGEE DR16 and 17. Román-Zúñiga et al. (2023) identified a sample of 3360 young stars, for which they derived T_{eff}, $\log g$, [Fe/H], $L_\star$, $M_\star$, and age using tools separate from the standard APOGEE pipeline. There are 168 main-sequence and 251 pre-main-sequence stars that overlap with our sample. As illustrated in Figure 3, we found that our photometrically derived T_{eff} values are consistent with those derived from APOGEE spectra. However, for stars brighter than $\log L_\odot \approx -1$, Román-Zúñiga et al. (2023) derived increasingly larger luminosities; the effect of higher luminosities can be seen propagated into the derivation of higher stellar radii. We attribute this disagreement in the luminosity and radii of earlier-type stars to the specific manner in which extinction is taken into account in the two works since the difference in T_{eff} (∼150 K) between the two works is not significant enough to make a difference in the derivation of the radii, and both works use Gaia DR3 magnitudes. While our work relies on more recent dust maps from Green et al. (2019) and Schlafly & Finkbeiner (2011), Román-Zúñiga et al. (2023) took a more empirical approach and did not use dust maps. They estimated the visual extinction for each source and established a
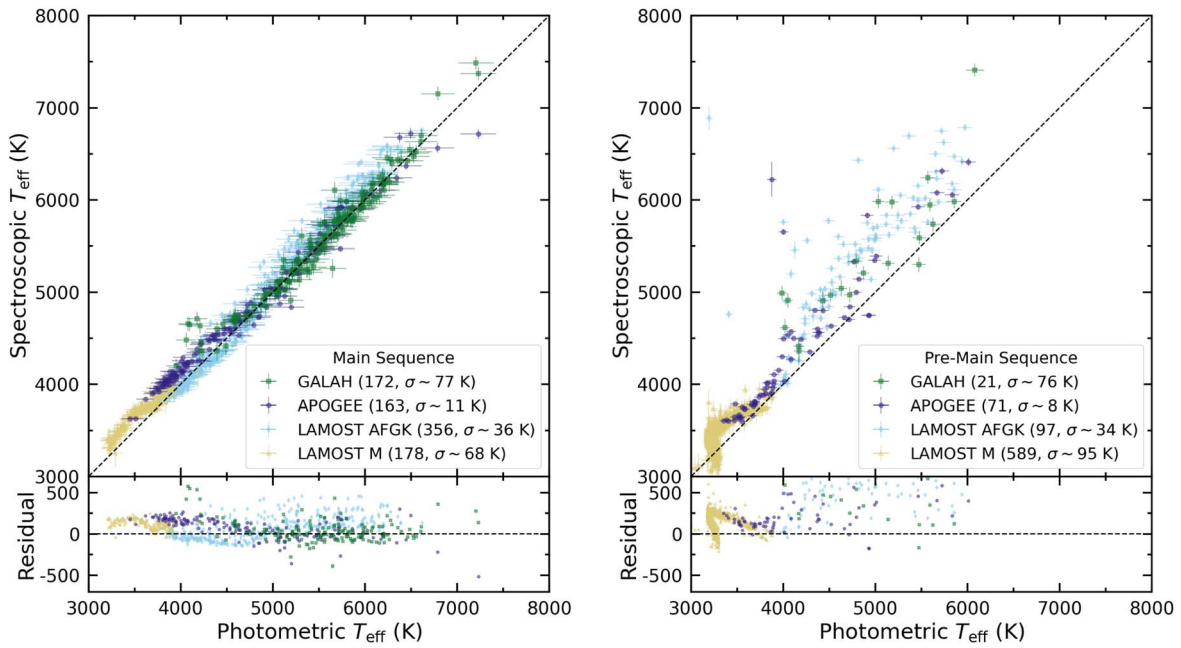
Figure 2. Comparison between spectroscopically derived T_{eff} from GALAH, APOGEE, and LAMOST and our photometrically derived T_{eff} values for both main-sequence fitting (left) and pre-main-sequence fitting (right). For each survey, we list the number of targets and the median spectroscopic T_{eff} uncertainty in parentheses.

confidence range through a Monte Carlo method. This was achieved by minimizing the differences between the extinction-corrected colors and the expected intrinsic colors from Luhman (2020). To correct the observed colors, they applied the extinction law of Cardelli et al. (1989), assuming a canonical interstellar reddening law with $R_v = 3.1$ for all regions. Their luminosities were derived using the extinction-corrected J magnitude, the bolometric correction for pre-main-sequence stars from PM13, and Gaia EDR3 geometric distance estimations from Bailer-Jones et al. (2021). Román-Zúñiga et al. (2023) derived their masses via Monte Carlo sampling and interpolation within the PARSEC-COLIBRI evolutionary model grid (Bressan et al. 2012). We did, however, find that main-sequence mass measurements are consistent with a median offset of $0.004 M_\odot$, well below our typical measurement uncertainty of $0.058 M_\odot$. For pre-main-sequence stars, our masses derived using magnetic isochrones are visually more consistent with those derived by Román-Zúñiga et al. (2023); however, for stars in the range of M-dwarf masses ($\lesssim 0.6 M_\odot$), the isochronal mass uncertainties are very large (see Figure 3).

Our comparisons with spectroscopically derived properties show reasonable agreement, with some deviations that we attribute to different methodology such as how we accounted for extinction or stellar model grids. Our measurements can be improved in the future with a large uniform spectroscopic survey of thousands of young stars with a wide range of ages and across all spectral types.

3.2. Main-sequence versus Pre-main-sequence Stellar Properties

We also compared the stellar properties between our pre-main-sequence and main-sequence populations (see Figure 4). It is important to note that the median age of the stars in our sample is ~45–50 Myr, at which point a majority of the M dwarfs have not yet reached the main sequence. As such, our sample has a much larger number of pre-main-sequence M

dwarfs than main-sequence M dwarfs. Overall, we see a significant decrease in the fraction of pre-main-sequence earlier-type stars. Comparing stellar masses, specifically in the $0.1–0.5 M_\odot$ region, we found that masses derived using nonmagnetic stellar isochrones were lower by ~50% compared to those derived using magnetic stellar isochrones. This is consistent with Simon et al. (2019), who found that nonmagnetic stellar isochrones do not properly account for the strong magnetic processes dominant in lower-mass stars. It is also important to note that for stars with $M_\star > 0.5 M_\odot$ the pre-main-sequence masses derived from nonmagnetic stellar isochrones match those derived using nonmagnetic stellar isochrones and follow the same overall distribution as the main-sequence masses.

4. The Effect of Stellar Properties on Survey Completeness

The intrinsic occurrence rate of planets (η) can be calculated from the fraction of stars with detected planets in a survey and the survey completeness as follows:

$$\eta = \frac{n_p}{n_\star} \times \frac{1}{\text{comp}_{bin}}, \qquad (4)$$

where comp_{bin} is the survey completeness evaluated in a discrete radius and orbital period bin, n_p is the number of detected planets in the bin, and $n_\star$ is the number of surveyed stars. The survey completeness is computed by combining the detection efficiency (calculated using injection-recovery tests) and the geometric transit probability, which is given by

$$f_{geo} = \frac{R_\star}{a}, \qquad (5)$$

where $R_\star$ is the stellar radius and a is the average semimajor axis, which is calculated from the orbital period using Kepler's third law. The uncertainty on the occurrence rate was calculated from the square root of the number of detected planets in the bin, assuming Poisson statistics.
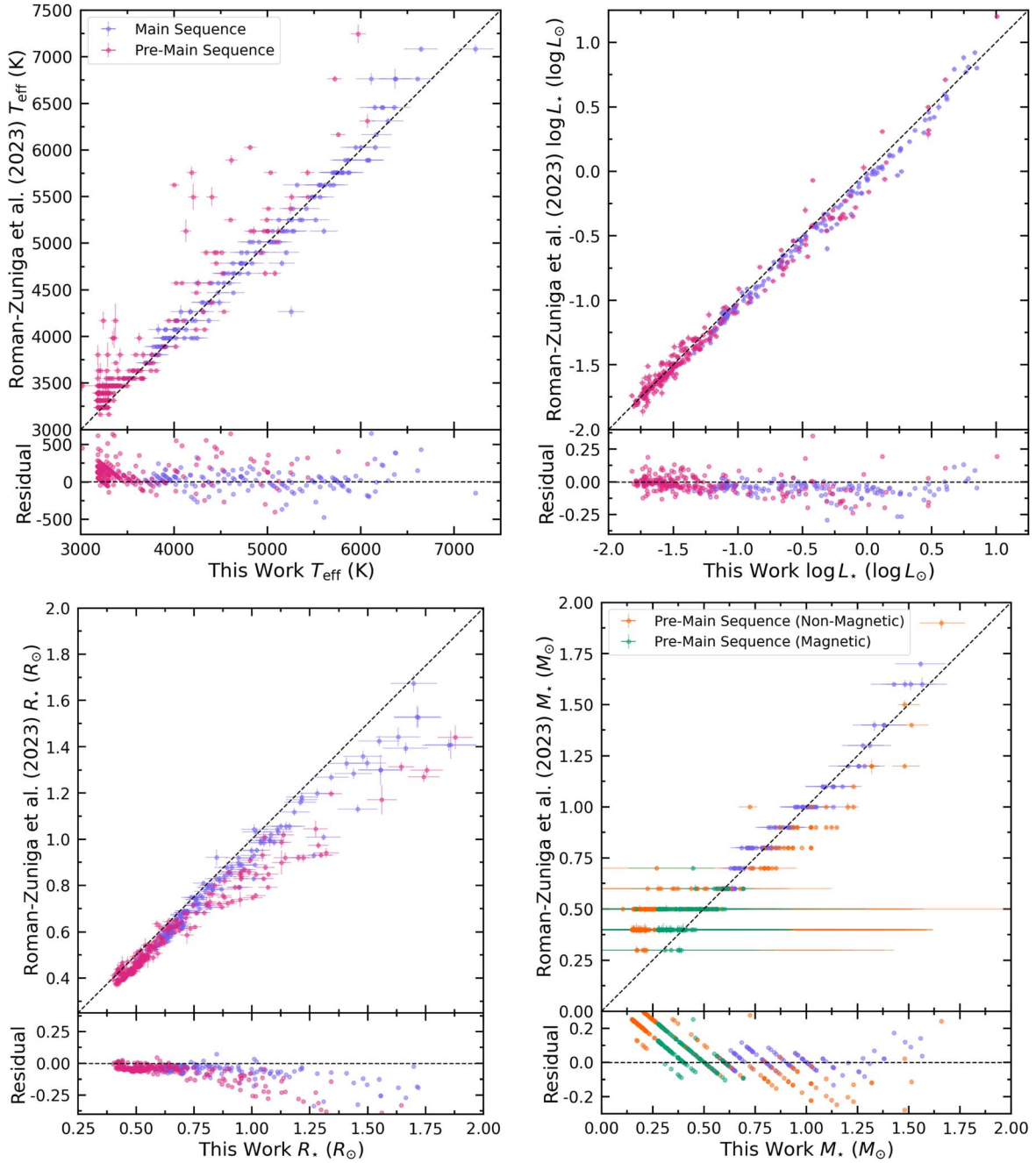
Figure 3. Comparison between spectroscopically derived T_{eff}, luminosity, stellar radius, and mass derived from APOGEE spectra as in Román-Zúñiga et al. (2023) and our photometrically derived T_{eff} values for both main-sequence and pre-main-sequence stars.

In our preliminary analysis of short-period planets in young clusters (Fernandes et al. 2022), we searched five clusters with 10 known transiting planets: Tucana–Horologium association, IC 2602, Upper Centaurus Lupus, Ursa Major, and Pisces-Eridanus. We ran the TESS Primary Mission Full Frame Images (FFIs; 30-minute cadence) through our pipeline `pterodactyls` (Fernandes 2022) and recovered seven of the eight confirmed planets and one of the two planet candidates. Here, it is important to reiterate that these clusters were solely selected to be used as a test sample to evaluate the effectiveness of our code in recovering these known planets. We specifically focused on sub-Neptunes and Neptunes (0.017–$0.055 \frac{R_p}{R_\star}$ or 1.8–$6\,R_\oplus$, assuming a solar radius for the host star) with orbital periods <12.5 days (about half a TESS

sector) to better understand the primordial population of sub-Neptunes and Neptunes before they are stripped of their atmospheres. Using Gaia, we took into account the flux contamination prominent in young cluster environments and computed our detection efficiency in $\frac{R_p}{R_\star}$ space because, at the time, most stars in our clusters lacked stellar properties. Given the lack of a homogeneous stellar catalog, we previously included stars of all spectral types in the analysis of our detection efficiency. With an average detection efficiency of 9% and geometric transit probability (f_{geo}) of 0.1 (at a geometric mean orbital period of 3.5 days and assuming a solar-type star), we computed an occurrence rate of $49\% \pm 20\%$ for sub-Neptunes and Neptunes in our biased sample of young clusters. This is much higher than the Kepler
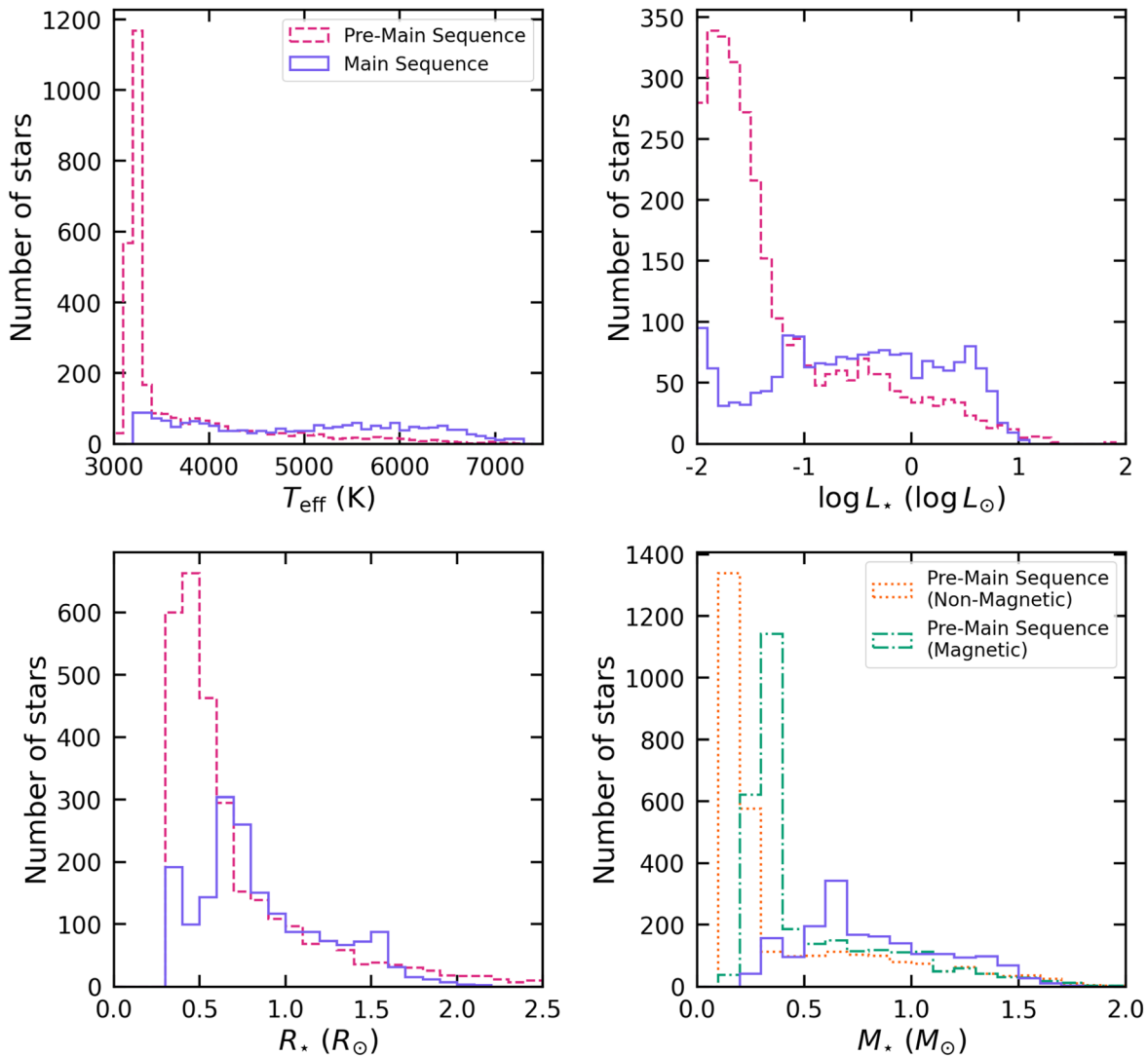
Figure 4. Histograms comparing the stellar properties of our pre-main-sequence and main-sequence stars showing effective temperatures (top left), luminosities (top right), radii (bottom left), and masses (bottom right). In all panels, the main-sequence distribution is depicted in purple. For the effective temperature, luminosity, and radius panels, the pre-main-sequence distribution is in pink. In the mass panel, we show the pre-main-sequence masses from nonmagnetic (orange) and magnetic (green) stellar isochrones to highlight the different distributions.

Gyr-old FGK (Sun-like) occurrence rate of 6.8% ± 0.3% in the same planet radius and orbital period bin. In this section, we revisited that number using the radii and masses calculated from our homogeneous approach.

In this paper, we computed stellar properties for 660 out of 1357 stars studied in Fernandes et al. (2022), with the remaining stars being too faint or lacking necessary 2MASS and Gaia DR3 photometry. After revising our sub-Neptune and Neptune regime detection efficiency with these updated stellar properties, we found a slight increase in the average detection efficiency from 9% to 10% (Figure 5). However, since the total number of stars decreased by 50%, the occurrence rate of sub-Neptunes and Neptunes increased to 90% ± 37%. For a better comparison with Kepler's Gyr-old planet population orbiting Sun-like stars, we analyzed only young stars of FGK spectral type (426 stars; 0.55–1.63 $M_\odot$). We observed an average detection efficiency of 15% in the young sub-Neptune and Neptune regime, leading to an occurrence rate of 93% ± 38%. This is comparable to the 90% ± 37% for all spectral types, which may be partially due to the removal of faint M-dwarf

stars that make it harder to detect transiting planets with TESS (Kunimoto et al. 2022).

While this occurrence rate is indeed higher than that of Kepler's Gyr-old population, even when accounting for the fraction of evaporated sub-Neptunes (Bergsten et al. 2022), it is still heavily biased given that we only looked at clusters that are known to have planets. As such, including clusters without known detected planets would lead to a lower occurrence rate. In fact, given that we now know that there are ∼2300 Sun-like stars and 15 published planets in our sample of nearby (<200 pc) young clusters and moving groups, assuming the same detection efficiency, the occurrence would drop to 43% ± 11%, which is effectively the same as the value of 49% ± 20% that we computed in Fernandes et al. (2022). This observed increase in the occurrence rate of sub-Neptunes and Neptunes could indicate a surplus of these planets at young ages. In future work, as we expand our sample to include data from all nearby clusters and moving groups, it will be important to determine whether this increase in occurrence rate persists when working with a nonbiased sample. If it does, it could be due to the fact that the atmospheres of these young
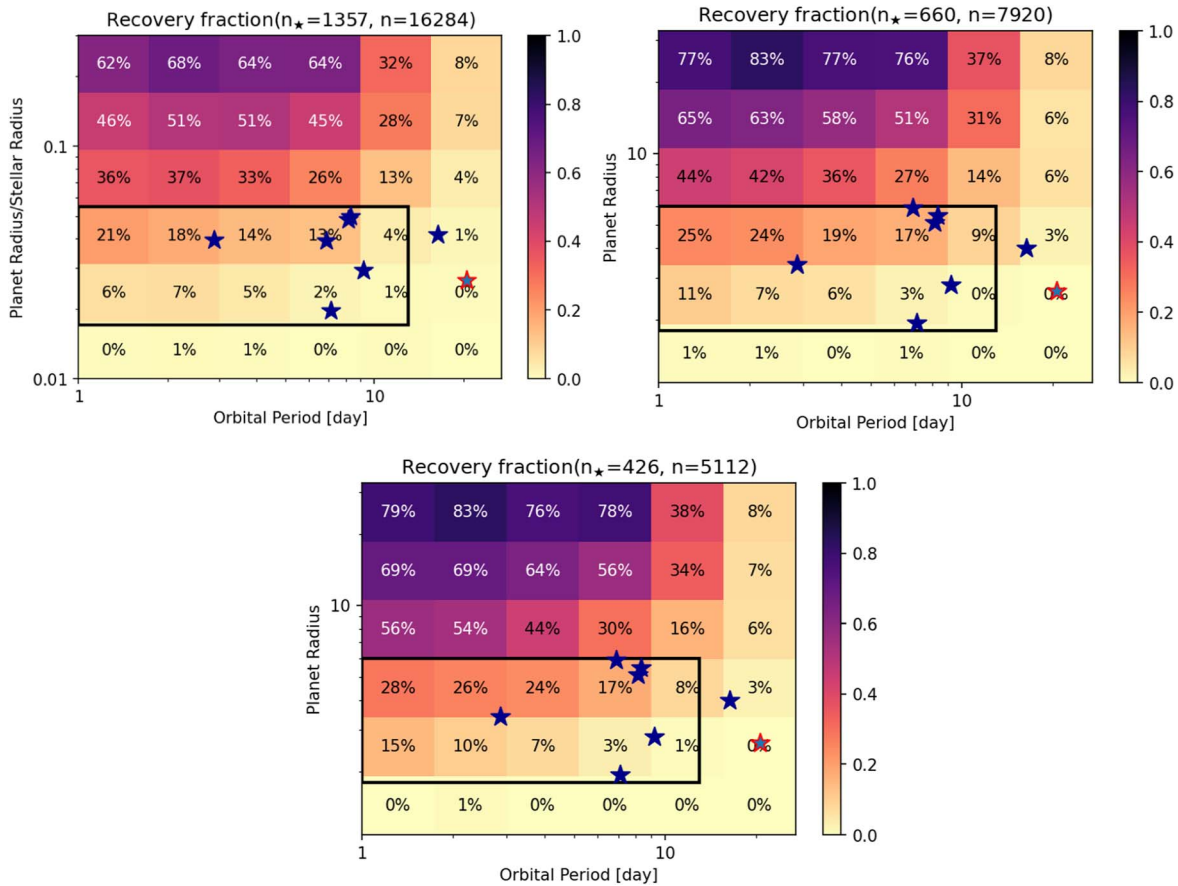
Figure 5. Comparison of detection efficiencies of the sample analyzed in Fernandes et al. (2022). The confirmed planets are depicted using blue stars, except for TOI 1726b, whose recovery required changing `pterodactyls`. Darker bins represent regions of higher detection efficiency. Parameter $n_\star$ is the total number of stars in our sample, while n is the total number of injections done. The black box denotes the bin over which the intrinsic occurrence rates were calculated, i.e., sub-Neptunes and Neptunes (0.017–0.055 $\frac{R_p}{R_\star}$ or 1.8–6 $R_\oplus$, assuming a solar radius) within an orbital period of 12.5 days (about half a TESS sector). Top left: detection efficiency of all 1357 stars in $\frac{R_p}{R_\star}$–period space before stellar characterization. Top right: detection efficiency in planet radius–orbital period space of 660 stars for which we were able to compute stellar properties. Bottom: detection efficiency in planet radius–orbital period space of 426 FGK (0.55–1.63 $M_\odot$) stars.

sub-Neptunes and Neptunes have not yet been stripped by photoevaporation or core-powered mass loss.

5. Summary and Discussion

The discovery and characterization of transiting exoplanets are strongly dependent on our understanding of their host star properties. In this paper, we used Gaia and 2MASS photometry along with stellar (magnetic and nonmagnetic) isochrones in order to derive a homogeneous set of stellar properties, specifically $T_{\rm eff}$, $L_\star$, $R_\star$, and $M_\star$ for 4865 stars (1824 main-sequence, and 3041 pre-main-sequence) from 31 nearby ($\sim$200 pc) young ($<$1 Gyr) clusters and moving groups. We found the following:

1. Our photometrically derived $T_{\rm eff}$ values generally agree within measurement uncertainties with those derived from spectroscopic surveys APOGEE, GALAH, and LAMOST for both main-sequence populations. There are some discrepancies, however, for pre-main-sequence stars, which we attribute to spectroscopic surveys using stellar models tuned to main-sequence stars.

2. Our $T_{\rm eff}$ values typically agree within measurement uncertainties with those derived in Román-Zúñiga et al. (2023) using APOGEE spectra. Our non-M-dwarf luminosities and radii increasingly deviate toward earlier-type stars, which we attribute to differences in accounting for interstellar extinction.

3. For FGK-type stars, we found that there was no difference in the masses derived from nonmagnetic versus magnetic stellar isochrones. On the other hand, for pre-main-sequence M dwarfs (0.1–0.5 $M_\odot$), our masses derived from magnetic stellar isochrones are visually more consistent with those derived in Román-Zúñiga et al. (2023); however, our measurement uncertainties are on the order of 100% for this population, making it difficult to conclusively rule out nonmagnetic measurements. However, Simon et al. (2019) found that nonmagnetic stellar isochrones tend to underestimate stellar masses, which is consistent with what we see here.

4. Given that the median age of our sample is $\sim$45–50 Myr, most of the M dwarfs in our sample have not yet reached the main sequence. We also note a marked decrease in the number of earlier-type pre-main-sequence stars with respect to main-sequence stars.

5. When we took stellar properties into account, there is an overall increase in our detection efficiency. This effect is particularly noticeable among sub-Neptunes/Neptunes (1.8–6 $R_\oplus$), where we found a $1.5\times$ increase in the detection efficiency, implying that better characterization

of host star properties can lead to the recovery of more smaller transiting planets.

The occurrence rate of sub-Neptunes/Neptunes (1.8–6 $R_\oplus$) with orbital periods less than 12.5 days for the 660 stars (out of 1357) for which we could compute stellar properties is $90\% \pm 37\%$. This is significantly higher than Kepler's Gyr-old occurrence rate of $6.8\% \pm 0.3\%$ even when accounting for evaporated sub-Neptunes (Bergsten et al. 2022), as well as our previously calculated $49\% \pm 20\%$ (Fernandes et al. 2022) when considering stars of all spectral types in $\frac{R_p}{R_\star}$ space. When considering only young stars of FGK spectral type (426 stars; 0.55–1.63 $M_\odot$), we computed an occurrence of $93\% \pm 38\%$, which is effectively the same as $90\% \pm 37\%$ when considering all stars with stellar properties. While the number of detected planets has not changed, the difference can be attributed to two factors: (1) the total number of only FGK stars is ∼1.5 times lower, and (2) the detection efficiency is ∼1.5 times higher. While the planet occurrence rate we calculated for our sample is higher than that for Kepler's Gyr-oldstars, we realize that this value is biased since we only considered clusters with confirmed/candidate planets. We can further improve on this by including all of the >30 young short-period transiting planets, as well as an unbiased sample of nearby clusters and moving groups using light curves from the TESS Extended Mission FFIs. Our homogeneously derived catalog of updated stellar properties will be a crucial input to the accurate estimation of the occurrence rates of young planets. With this young population of transiting, short-period planets, we hope to improve on the intrinsic occurrence rate calculations, establish how the radius distribution of transiting exoplanets evolved over time, and therefore provide observational constraints on the mass-loss mechanisms of planetary atmospheres.

Appendix
Summary of Young Clusters and Moving Groups

In Table 3, we relied on known members of young clusters, associations and moving groups whose distance, age, and membership are from Gagné et al. (2018) and Babusiaux et al. (2018).

Table 3
Moving Groups and Clusters Whose Properties Were Derived in This Work

Cluster/Moving Group	Distance (in pc)	Age (in Myr)	Total	No. in Gaia	No. in 2MASS	No. in PMS	No. in MS
118 Tau	100 ± 10	∼10	15	15	15	4	3
32 Ori	96 ± 2	22^{+4}_{-3}	42	41	41	5	8
AB Doradus MG	30^{+20}_{-10}	149^{+51}_{-19}	596	594	539	79	113
Alpha Persei	∼200	90	740	740	717	368	75
Argus	∼120	40-50	38	38	37	5	14
Beta Pictoris	30^{+20}_{-10}	24 ± 3	303	302	271	69	51
Blanco 1	253	132	489	489	481	98	189
Carina	60 ± 20	30^{+11}_{-7}	123	123	114	46	12
CarinaNear	30 ± 20	∼200	183	183	161	20	27
Coma Bernices	∼85	562^{+98}_{-84}	165	165	160	4	64
Columba	50 ± 20	42^{+6}_{-4}	220	220	200	49	44
Eta Cha	95 ± 1	11 ± 3	18	18	18	7	0
Hyades	40-50	750 ± 100	612	612	573	91	146
IC 2391	149 ± 6	50 ± 5	333	333	328	151	34
IC 2602	149 ± 5	46^{+6}_{-5}	504	504	477	253	29
Lower Centaurus Crux	110 ± 10	15 ± 3	530	529	500	144	62
Mu Tau	150	60	566	566	509	143	70
NGC 2451	180-360	50-80	400	400	380	197	35
Octans	130^{+30}_{-20}	35 ± 5	159	159	151	32	40
Pisces-Eridanus	80- 226	120	254	254	250	48	114

Table 3
(Continued)

Cluster/Moving Group	Distance (in pc)	Age (in Myr)	Total	No. in Gaia	No. in 2MASS	No. in PMS	No. in MS
Platais 8	130 ± 10	60	35	35	33	4	12
Pleiades	134 ± 9	112 ± 5	1593	1590	1545	467	253
Praesepe	179 ± 3	790 ± 60	860	860	835	226	265
Tucana–Horologium association	46^{+8}_{-6}	45 ± 4	212	211	205	85	15
TW Hydra	60 ± 10	10 ± 3	86	86	73	17	2
Upper Centaurus Lupus	130 ± 20	16 ± 2	936	934	903	248	101
Upper CrA	147 ± 7	~ 10	41	41	38	21	1
Ursa Major	~ 25	414 ± 23	17	17	16	0	5
Upper Scorpius	130 ± 20	10 ± 3	411	411	395	149	10
Volans Carina	75-100	89^{+5}_{-7}	86	86	82	8	25
XFOR	~ 100	~ 40	17	17	17	3	5
Total			10,585	10,573	10,064	3041	1824

Note. Distance, age, and membership are from Gagné et al. (2018) and Babusiaux et al. (2018).

ORCID iDs

Rachel B. Fernandes ● https://orcid.org/0000-0002-3853-7327
Kevin K. Hardegree-Ullman ● https://orcid.org/0000-0003-3702-0382
Ilaria Pascucci ● https://orcid.org/0000-0001-7962-1683
Galen J. Bergsten ● https://orcid.org/0000-0003-4500-8850
Gijs D. Mulders ● https://orcid.org/0000-0002-1078-9493
Katia Cunha ● https://orcid.org/0000-0001-6476-0576
Eric E. Mamajek ● https://orcid.org/0000-0003-2008-1488
Kyle A. Pearson ● https://orcid.org/0000-0002-5785-9073
Gregory A. Feiden ● https://orcid.org/0000-0002-2012-7215
Jason L. Curtis ● https://orcid.org/0000-0002-2792-134X

References

Abdurrouf, Accetta, K., & Aerts, C. 2022, ApJS, 259, 35
Andrae, R., Fouesneau, M., Creevey, O., et al. 2018, A&A, 616, A8
Babusiaux, C., van Leeuwen, F., Barstow, M., et al. 2018, A&A, 616, A10
Bailer-Jones, C. A. L., Rybizki, J., Fouesneau, M., Demleitner, M., & Andrae, R. 2021, AJ, 161, 147
Berger, T. A., Huber, D., van Saders, J. L., et al. 2020, AJ, 159, 280
Bergsten, G. J., Pascucci, I., Mulders, G. D., Fernandes, R. B., & Koskinen, T. T. 2022, AJ, 164, 190
Borucki, W. J., Koch, D., Basri, G., et al. 2010, Sci, 327, 977
Bouma, L., Hartman, J., Brahm, R., et al. 2020, AJ, 160, 239
Bressan, A., Marigo, P., Girardi, L., et al. 2012, MNRAS, 427, 127
Brown, T. M., Latham, D. W., Everett, M. E., & Esquerdo, G. A. 2011, AJ, 142, 112
Buder, S., Sharma, S., Kos, J., et al. 2021, MNRAS, 506, 150
Busso, G., Cacciari, C., Bellazzini, M., et al. 2021, Gaia DR3 Documentation, European Space Agency, 5
Cardelli, J. A., Clayton, G. C., & Mathis, J. S. 1989, ApJ, 345, 245
Cody, A. M., Stauffer, J., Baglin, A., et al. 2014, AJ, 147, 82
Cui, X. Q., Zhao, Y. H., Chu, Y. Q., et al. 2012, RAA, 12, 1197
Curtis, J. L., Agüeros, M. A., Mamajek, E. E., Wright, J. T., & Cummings, J. D. 2019, AJ, 158, 77
Dietrich, J., Apai, D., Schlecker, M., et al. 2023, AJ, 165, 149
Dressing, C. D., Hardegree-Ullman, K., Schlieder, J. E., et al. 2019, AJ, 158, 87
Duchêne, G., & Kraus, A. 2013, ARA&A, 51, 269
El-Badry, K., Rix, H. W., & Heintz, T. M. 2021, MNRAS, 506, 2269
Ercolano, B., & Pascucci, I. 2017, RSOS, 4, 170114
Fang, M., Kim, J. S., Pascucci, I., & Apai, D. 2021, ApJ, 908, 49
Fang, M., Pascucci, I., Edwards, S., et al. 2023, ApJ, 945, 112
Feiden, G. A. 2016, A&A, 593, A99
Feinstein, A. D., Montet, B. T., Foreman-Mackey, D., et al. 2019, PASP, 131, 094502

Fernandes, R. 2022, pterodactyls: A Tool to Uniformly Search and Vet for Young Transiting Planets In TESS Primary Mission Photometry, v0.1, Zenodo, doi:10.5281/zenodo.6667960
Fernandes, R. B., Mulders, G. D., Pascucci, I., et al. 2022, AJ, 164, 78
Fulton, B. J., Petigura, E. A., Howard, A. W., et al. 2017, AJ, 154, 109
Gaia Collaboration, Arenou, F., & Babusiaux, C. 2023a, A&A, 674, A34
Gaia Collaboration, Brown, A. G. A., & Vallenari, A. 2018, A&A, 616, A1
Gaia Collaboration, Brown, A. G. A., & Vallenari, A. 2021, A&A, 649, A1
Gaia Collaboration, Prusti, T., & de Bruijne, J. H. J. 2016, A&A, 595, A1
Gaia Collaboration, Vallenari, A., & Brown, A. G. A. 2023b, A&A, 674, A1
Gagné, J., David, T. J., Mamajek, E. E., et al. 2020, ApJ, 903, 96
Gagné, J., Mamajek, E. E., Malo, L., et al. 2018, ApJ, 856, 23
Giacalone, S., Dressing, C. D., Jensen, E. L. N., et al. 2021, AJ, 161, 24
Ginzburg, S., Schlichting, H. E., & Sari, R. 2016, ApJ, 825, 29
Ginzburg, S., Schlichting, H. E., & Sari, R. 2018, MNRAS, 476, 759
Green, G. M. 2018, JOSS, 3, 695
Green, G. M., Schlafly, E., Zucker, C., Speagle, J. S., & Finkbeiner, D. 2019, ApJ, 887, 93
Gupta, A., & Schlichting, H. E. 2019, MNRAS, 487, 24
Gupta, A., & Schlichting, H. E. 2020, MNRAS, 493, 792
Hardegree-Ullman, K. K., Zink, J. K., Christiansen, J. L., et al. 2020, ApJS, 247, 28
Hedges, C. 2021, RNAAS, 5, 262
Hertzsprung, E. 1911, POPot, 63, 22
Hippke, M., David, T. J., Mulders, G. D., & Heller, R. 2019, AJ, 158, 143
Hippke, M., & Heller, R. 2019, A&A, 623, A39
Howell, S. B., Sobeck, C., Haas, M., et al. 2014, PASP, 126, 398
Huber, D., Bryson, S. T., Haas, M. R., et al. 2016, ApJS, 224, 2
Hunter, J. D. 2007, CSE, 9, 90
Jones, E., Oliphant, T., Peterson, P., et al. 2001, SciPy: Open source scientific tools for Python, http://www.scipy.org/
Kunimoto, M., Daylan, T., Guerrero, N., et al. 2022, ApJS, 259, 33
Luhman, K. L. 2020, AJ, 160, 186
Mamajek, E. E., Torres, G., Prsa, A., et al. 2015, arXiv:1510.06262
Mann, A. W., Dupuy, T., Kraus, A. L., et al. 2019, ApJ, 871, 63
Mann, A. W., Feiden, G. A., Gaidos, E., Boyajian, T., & von Braun, K. 2015, ApJ, 804, 64
Mann, A. W., Johnson, M. C., Vanderburg, A., et al. 2020, AJ, 160, 179
Mulders, G. D., Pascucci, I., Apai, D., & Ciesla, F. J. 2018, AJ, 156, 24
Nardiello, D., Piotto, G., Deleuil, M., et al. 2020, MNRAS, 495, 4924
Newton, E. R., Mann, A. W., Kraus, A. L., et al. 2021, AJ, 161, 65
Newton, E. R., Mann, A. W., Tofflemire, B. M., et al. 2019, ApJL, 880, L17
Owen, J. E., & Wu, Y. 2013, ApJ, 775, 105
Owen, J. E., & Wu, Y. 2017, ApJ, 847, 29
Pascucci, I., Testi, L., Herczeg, G. J., et al. 2016, ApJ, 831, 125
Pecaut, M. J., & Mamajek, E. E. 2013, ApJS, 208, 9
Ricker, G. R., Winn, J. N., Vanderspek, R., et al. 2014, JATIS, 1, 014003
Rizzuto, A. C., Newton, E. R., Mann, A. W., et al. 2020, AJ, 160, 33
Rogers, J. G., Gupta, A., Owen, J. E., & Schlichting, H. E. 2021, MNRAS, 508, 5886
Román-Zúñiga, C. G., Kounkel, M., Hernández, J., et al. 2023, AJ, 165, 51
Russell, H. N. 1914, PA, 22, 275

Salama, M., Ziegler, C., Baranec, C., et al. 2022, AJ, 163, 200
Schlafly, E. F., & Finkbeiner, D. P. 2011, ApJ, 737, 103
Schlegel, D. J., Finkbeiner, D. P., & Davis, M. 1998, ApJ, 500, 525
Simon, M., Guilloteau, S., Beck, T. L., et al. 2019, ApJ, 884, 42
Skrutskie, M. F., Cutri, R. M., Stiening, R., et al. 2006, AJ, 131, 1163
Stassun, K. G., Oelkers, R. J., Paegert, M., et al. 2019, AJ, 158, 138
Stassun, K. G., Oelkers, R. J., Pepper, J., et al. 2018, AJ, 156, 102
Torres, G., Andersen, J., & Giménez, A. 2010, A&ARv, 18, 67

van der Walt, S., Colbert, S. C., & Varoquaux, G. 2011, CSE, 13, 22
Van Eylen, V., Agentoft, C., Lundkvist, M., et al. 2018, MNRAS, 479, 4786
Wang, S., & Chen, X. 2019, ApJ, 877, 116
Zellem, R. T., Pearson, K. A., Blaser, E., et al. 2020, PASP, 132, 054401
Ziegler, C., Tokovinin, A., Briceño, C., et al. 2020, AJ, 159, 19
Zink, J. 2019, jonzink/EDI-Vetter: Initial Release, v1.0, Zenodo, doi:10.5281/zenodo.3585940
Zuckerman, B. 2019, ApJ, 870, 27